



Research Paper

Highly enhanced photocatalytic activity of $\text{CaSn}(\text{OH})_6$ through tuning $\text{CaSn}(\text{OH})_6/\text{SnO}_2$ heterostructural interaction and optimizing Fe^{3+} doping concentration



Tongyao Liu^a, Xinlong Ma^a, Linfen Yang^a, Hao Li^a, Huihui Li^a, Soo Wohn Lee^b, Yuhua Wang^{a,*}

^a Department of Materials Science, School of Physical Science and Technology, Lanzhou University, Lanzhou, 730000, China

^b Sunmoon University, 100, GalSan-Ri, TangJung-Myon, Asan, ChungNam, 336-708, Republic of Korea

ARTICLE INFO

Article history:

Received 23 February 2017

Received in revised form 22 April 2017

Accepted 27 May 2017

Available online 1 June 2017

Keywords:

Photocatalysis

UV-vis light

Heterostructures

Fe^{3+} ions doping

ABSTRACT

A series of novel $\text{CaSn}(\text{OH})_6/\text{SnO}_2$ heterostructure (CSH) photocatalysts have been synthesized via a facile one-pot hydrothermal process with different molar ratios of raw materials. The obtained $\text{CaSn}(\text{OH})_6/\text{SnO}_2$ composite with $\text{CaCl}_2:\text{SnCl}_4 = 0.8$ (0.8CSH) exhibits outstanding ultraviolet (UV)-light photocatalytic activity, which could be attributed to the efficient separation of photogenerated electrons and holes. Meanwhile, the doping of Fe^{3+} ions into 0.8CSH substrate greatly enhances the UV and visible-light photocatalytic activities, and the photodegradation rate of 1.0 mol% Fe-doped CSH (1.0FCSH) sample exceeds that of 0.8CSH by a factor of more than 14 times. This could be attributed to the fact that Fe-doping induces the shift of the absorption edge into the visible light region and reduces the recombination of electron-hole pairs. Overall, this research can provide an effective approach to synthesize new efficient photocatalysts and facilitate their application in environmental protection.

© 2017 Elsevier B.V. All rights reserved.

1. Introduction

The shortage of energy source and the increasing amount of harmful effluent are the two emergency issues confronting humanity at present. Photocatalytic reactions, including degradation of organic pollutants, H_2 evolution and photocatalytic CO_2 reduction, have attracted extensive interests [1–3]. Among various photocatalyst materials, perovskite oxides such as SrTiO_3 [4], NaTaO_3 [5], and BiFeO_3 [6] are prominent in their broad diversity, owing to their good stability, simple structure and outstanding photocatalytic ability [7,8]. Meanwhile, some hydroxide-based photocatalysts, such as $\text{In}(\text{OH})_3$ and layered double hydroxides (LDHs), have been widely employed in photodegradation of pollutants [9–11]. Actually, one of the main reasons is that the plenty of surface OH groups will combine photogenerated holes to form hydroxyl radicals ($\cdot\text{OH}$), which are the main oxidants to decompose the pollutants even stubborn benzene [12].

$\text{CaSn}(\text{OH})_6$, a class of perovskite-type hydroxide, may have great potential to take both above advantages in photocatalysis. Further, the central Sn^{4+} ions possess d^{10} electronic structure, which is

beneficial for the separation of photogenerated electron-hole pairs [9,13]. The crystal structure of $\text{CaSn}(\text{OH})_6$ is built with the crystallographic data taken from ICSD-25825 and displayed in Fig. 1. Clearly, $\text{CaSn}(\text{OH})_6$ crystal presents an orthorhombic perovskite structure with a space group of Pn-3, and it is constructed of $\text{Ca}(\text{OH})_6$ and $\text{Sn}(\text{OH})_6$ octahedrons by sharing vertexes. More importantly, this framework can facilitate the mobility of the charged carriers, and then enhance the photocatalytic activity of $\text{CaSn}(\text{OH})_6$ under light irradiation [14]. Lately, cube-shaped $\text{CaSn}(\text{OH})_6$ photocatalyst has been prepared by Meng et al. via a facile sonochemical method and used directly as a UV light induced photocatalyst. However, its poor semiconductivity and low photodegradation rate inhibit the practical application in wastewater treatment [15]. Many reports demonstrate that the couple between two different semiconductors could accelerate interfacial charge transfer, thus inhibits the recombination of photogenerated carriers [16–18]. SnO_2 , a stable oxide with outstanding electrical and optical properties [19], is a good candidate as a coupled semiconductor to $\text{CaSn}(\text{OH})_6$, because of its suitable band positions with $\text{CaSn}(\text{OH})_6$. Meanwhile, the tunable composition as well as tight combination can be easily realized via one-pot hydrothermal method [20]. In this way, the enhanced separation of photogenerated electrons and holes is expected. Nevertheless, pure $\text{CaSn}(\text{OH})_6$ and SnO_2 photocatalysts both cannot utilize visible light directly because of their wide band gap energies

* Corresponding author.

E-mail address: wyh@lzu.edu.cn (Y. Wang).

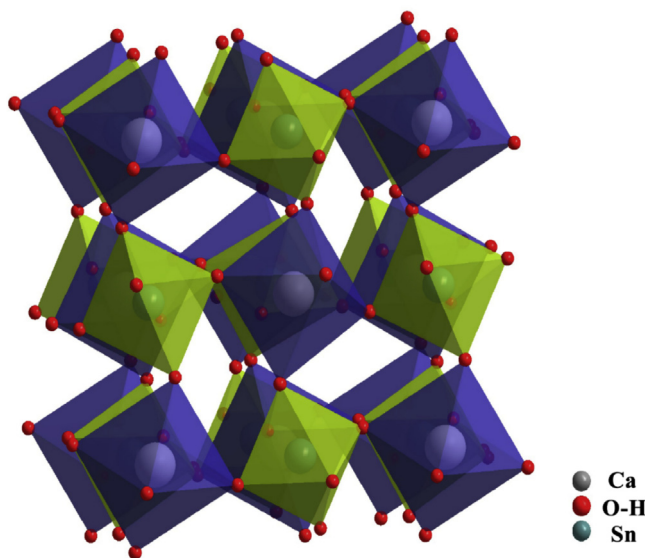


Fig. 1. The crystallographic structure of the $\text{CaSn}(\text{OH})_6$.

(larger than 3.0 eV) [15,21], which are similar to TiO_2 [22], ZnO [23] and other traditional UV-type photocatalysts. Therefore, extension of the light absorption to the visible light region (accounting for 45% of the total sunlight) is the key factor for improving the photocatalytic activity of $\text{CaSn}(\text{OH})_6$ and extending its practical application.

Transition metal ions doping is one of the typical approaches to extend the spectral response of the $\text{CaSn}(\text{OH})_6$ to the visible light region by introducing defect states in the band gap. For example, Baeissa has doped $\text{CaSn}(\text{OH})_6$ with Pd metal during the sonochemical method to allow the degradation of methylene blue (MB) solution under visible light [13]. However, the consumption of a large amount of noble metal immensely limits its practical applications. Some low-cost metal elements, like Fe [24], Mn [25], Ni [25], V [26], have been employed to tune the electronic structure and extend the photoresponse from the UV light region to the visible light region. Among them, Fe^{3+} ions have attracted special attention as a dopant because of its unique half-filled electron configuration [27]. For instance, Yu et al. have prepared Fe-doped TiO_2 nanorods via a hydrothermal method. This modification not only accelerates the shift of the absorption edge into visible light region, but also promotes the separation of photogenerated electron-hole pairs [24]. Song et al. synthesized Fe-doped WO_3 hollow sphere successfully and its visible light-driven photocatalytic activity has been remarkably enhanced, which could be attributed to the red shift of absorption edge and the trapping effect of the Fe-doped WO_3 [28]. As for CSH substrate, the matched ion radius between Sn^{4+} (0.069 nm) [29] and Fe^{3+} (0.064 nm) [30] will accelerate the substitution of Sn^{4+} in CSH substrate by Fe^{3+} . And then, the impurity energy level and shallow charge traps can be formed to extend the absorption region and reduce the electron-hole recombination, ultimately enhance the photocatalytic efficiency [24,31].

Inspired by the above discoveries, the design and preparation of $\text{CaSn}(\text{OH})_6$ -based photocatalysts have been carried out by two sequential steps. Firstly, the novel $\text{CaSn}(\text{OH})_6/\text{SnO}_2$ heterojunctions are synthesized by a facile one-pot hydrothermal process, and the photodegradation efficiency are evaluated to tune the optimal component ratio of $\text{CaSn}(\text{OH})_6$ and SnO_2 . Secondly, the doping of Fe^{3+} ions into the above optimal CSH sample has been implemented successfully. And the Fe-doped 0.8CSH samples (FCSH) show obvious visible light photocatalytic activity compared with 0.8CSH sample, indicating their considerable potential for application in environmental protection. Ultimately, based on the experimental

results, the possible mechanism for the enhanced photocatalytic activities of CSH and FCSH samples are proposed.

2. Experimental

2.1. Preparation of CSH cubes

CSH cubes are synthesized on the basis of a procedure reported previously [32]. All reagents are of analytical grade and used without further retreatment. The effect of the $\text{CaCl}_2/\text{SnCl}_4 \cdot 5\text{H}_2\text{O}$ (Ca/Sn) molar ratio on the composition of CSH has been investigated in detail. In a typical preparation, 0.4440 g CaCl_2 and 1.4024 g $\text{SnCl}_4 \cdot 5\text{H}_2\text{O}$ are dissolved in 15 mL deionized water under magnetic stirring (with a Ca/Sn molar ratio of 1.0) followed by adding 4.5 M NaOH solution to adjust pH into ~ 11 . After stirring for a further 120 min, the obtained white slurries are transferred into a stainless steel autoclave and hydrothermally treated at 180 °C for 24 h. The final products are obtained after being centrifuged and rinsed thoroughly with deionized water and ethanol. All of the samples are dried in air at 50 °C overnight before characterization. For convenience, the samples prepared with different Ca/Sn molar ratios of 0.6, 0.8, 1.0 and 1.2 are labelled as 0.6CSH, 0.8CSH, 1.0CSH and 1.2CSH, respectively.

2.2. Preparation of FCSH cubes

Similarly, a series of Fe-doped CSH photocatalysts are synthesized via an in situ preparation method. After the hydrothermal process of 0.8CSH substrate, moderate amount of $\text{FeCl}_2 \cdot 4\text{H}_2\text{O}$ are introduced into the Teflon-lined autoclave and reheated in 180 °C for one hour. After cooling down to room temperature, the gray products are centrifuged to separate solids and washed with deionized water and ethanol, and then dried at 50 °C overnight. The contents of Fe^{3+} ions in 0.8CSH skeleton are 0.5, 0.8, 1.0 and 1.5 mol%, corresponding to 0.5FCSH, 0.8FCSH, 1.0FCSH and 1.5FCSH, respectively.

2.3. Characterization

Powder X-ray diffraction (XRD) patterns are obtained on a Bruker D2 PHASER X-ray diffractometer using Cu K α radiation source ($\lambda = 1.54184 \text{ \AA}$) to determine the crystal phase of the obtained samples. The morphology of the sample and the energy dispersive X-ray spectroscopy (EDX) spectrum are detected by field emission scanning electron microscopy (FESEM, Hitachi, 30 S-3400N). The ultraviolet-visible (UV-vis) absorption spectra are obtained by a UV-Vis spectrophotometer (PE Lambda 950) with BaSO_4 as a reference. Besides, the energy dispersive X-ray spectroscopy (EDX) spectrum, transmission electron microscopy (TEM) and high-resolution transmission electron microscopy (HRTEM) images are collected on an F30 S-TWIN electron microscope (Tecnai G2, FEI Company). X-ray photoelectron spectroscopy (XPS, PHI-5702, Physical Electronics) is performed using a monochromatized Al K α irradiation. The contents of metal ions are analyzed using the inductively coupled plasma optical emission spectrometry (ICP-OES, PQ 9000). The chamber pressure is $\sim 3 \times 10^{-8}$ Torr under testing conditions. Photoluminescence (PL) spectra are measured at room temperature using a FLS-920T fluorescence spectrophotometer equipped with a 450 W Xe light source and double excitation monochromators. Thermogravimetric analyses (TGA) is performed using a TGA up to 800 °C (STA PT 1600, Linseis, Germany).

2.4. Evaluation of photocatalytic activity

The photocatalytic activities of CSH and FCSH are measured by the decomposition of methyl blue (MB) solution under various light

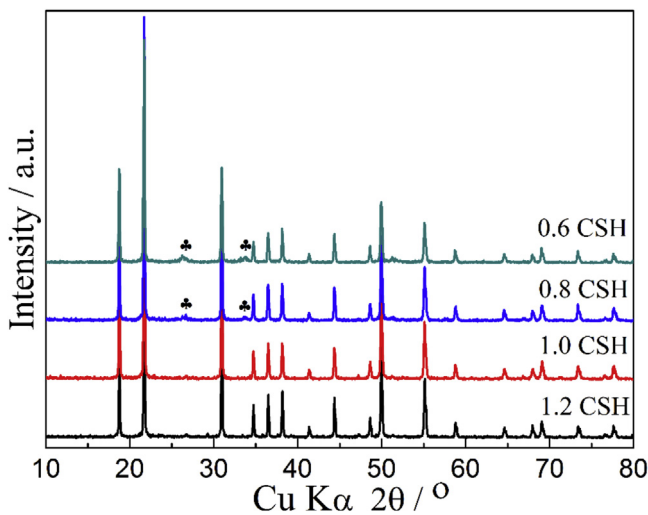


Fig. 2. XRD patterns of CSH samples synthesized with different Ca/Sn molar ratios.

irradiation. In CEL-LAB500 photochemical reaction instrument, 15.6 mg photocatalysts are suspended in the MB solution (10 mg/L, 25 mL). Before irradiation, the suspensions are stirred in the dark for 30 min to ensure the establishment of adsorption–desorption equilibrium. Then, a 500W Hg lamp or 350W Xe lamp equipped with a UV cutoff filter ($\lambda > 420$ nm) is irradiated to start the photocatalytic reaction. A series of certain volume of suspension are withdrawn at selected times for analysis, centrifuge suspension to obtain the supernatant fluid and the concentration of dye solution is analyzed by measuring the light absorption of the clear solution at 664 nm (λ_{max} for MB solution) using the UV–vis spectrophotometer (LG-722SP).

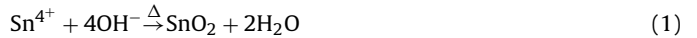
2.5. Photoelectrochemical measurements

Photocurrent are performed with an electrochemical analyzer (CS 310, Wuhan Correst Instrument Co. Ltd.) in a standard three-electrode system, composed of the CSH and FCSH samples (effective area is 1 cm²) as working electrodes, a Pt foil as the counter electrode and an Ag/AgCl (saturated KCl) electrode as a reference electrode. The photoanode is suspended into Na₂SO₄ (0.1 mol L⁻¹) aqueous solution with a 300W Xe arc lamp equipped with a UVREF filter (200–400 nm) and UVIRCUT filter (420–780 nm) served as the UV and visible light source, respectively. All measurements are carried out with light ON-OFF switches of 6 s at a constant potential of 0.1 V to the working electrode. The electrochemical impedance spectroscopies (EIS) of as-prepared samples are carried out at the open circuit potential. The frequency is ranging from 0.01 Hz to 100000 Hz and the amplitude of the sinusoidal wave is 10 mV. Furthermore, the flatband potentials (V_{fb}) are determined from Mott–Schottky plots by electrochemical method in Na₂SO₄ solution (0.1 mol L⁻¹) at a fixed frequency of 1000 Hz with 10 mV amplitude.

3. Results and discussion

The XRD patterns of as-prepared CSH samples with different Ca/Sn molar ratios are shown in Fig. 2. The peaks at 18.9°, 21.9° and 31.1° correspond to the (111), (200) and (220) crystal planes of cubic CaSn(OH)₆ (JCPDS 09-0030). Notably, with the decrease of Ca/Sn molar ratios, some trace peaks marked by “*” at 22.6° and 33.9° are checked in 0.6CSH and 0.8CSH samples, which are readily indexed to the diffraction peaks of SnO₂ (JCPDS 41-1445). This phe-

nomenon could be attributed to the hydrolysis of redundant Sn⁴⁺ in the alkaline solution (pH ~ 11), following Eq. (1).



However, as for 1.0CSH and 1.2CSH samples, diffraction peaks related to SnO₂ or other impurity phases no longer exist. This difference could be attributed to the complete reaction of CaCl₂ and SnCl₄, and the dissolution of CaCl₂ in the process of centrifugation with deionized water.

The morphology of as-prepared 0.8CSH sample (as typical sample) has been observed by SEM technique, as shown in Fig. 3a. Due to their intrinsic structures with cubic symmetry, the 0.8CSH samples are uniform cubes with the edge length of 3–5 μm. And the initial Ca/Sn molar ratios have nearly no effect on the morphologies of different samples (Fig. S1). As shown in Fig. 3b and c, it is clear that some nanoparticles are attached to the faces of microcubes, which indicates that the CaSn(OH)₆ microcubes may be formed by the adsorption of small CSH nanoparticles via the Oswald ripening mechanism [9,33]. Furthermore, combined with the HRTEM images of the magnified view (Fig. 3d and e), the distance of 0.286 nm between the adjacent lattice fringes can be assigned to the (220) planes of CaSn(OH)₆ crystals, while the distance of 0.264 nm and 0.335 nm can be assigned to the (101) and (110) planes of SnO₂ crystals, respectively. This result further confirms the co-existence of CaSn(OH)₆ and SnO₂ phases. Meanwhile, the tight interfacial contact between CaSn(OH)₆ and SnO₂ is expected to promote the synergistic effect of photocatalytic activity over CSH samples. In addition, EDX analysis confirms the distribution of Ca, Sn and O elements in 0.8CSH samples as depicted in Fig. 3f, which is corresponding to the results of XRD patterns.

The decomposition of MB solution under UV light irradiation are investigated to evaluate the photocatalytic activity of CSH, and the results are shown in Fig. 4a. Clearly, the photocatalytic degradation efficiency of MB solution follows the order 0.8CSH > 0.6CSH > 1.0CSH > 1.2CSH. As discussed above, with the decrease of Ca/Sn molar ratios below to 1.0, some SnO₂ particles will be generated and combined tightly with CaSn(OH)₆ cubes to exhibit synergistic photocatalysis effect. Therefore, the 0.8CSH sample shows much higher photodegradation ability than 1.0CSH and 1.2CSH samples. However, when the Ca/Sn molar ratio decreases to 0.6, there is an obvious reduction in photocatalytic activity. This result could be attributed to the fact that too much SnO₂ in the composites makes an unsuitable ratio between CaSn(OH)₆ and SnO₂, so as to generate lower electron transfer efficiency and lead to the poor response of the photocatalyst under UV light irradiation [34,35]. Based on previous studies, the degradation of dyes can be ascribed to a pseudo-first order reaction with a Langmuir–Hinshelwood model when the initial concentration of dye solution is small: $\ln(C_0/C) = kt$ (where C_0 and C are the concentration of MB solution at times 0 and t , t is the time of irradiation, and k is the first-order reaction rate constant) [36]. Fig. 4b exhibits the plots of $\ln(C_0/C)$ versus UV light irradiation time. Obviously, the apparent rate constant of 0.8CSH is 0.08376 min⁻¹, which is 1.48 and 1.91 times than that of 0.6CSH (0.05664 min⁻¹) and 1.0CSH (0.04384 min⁻¹), respectively. The distinguished photocatalytic capacity further confirms the most efficient synergistic effect of CaSn(OH)₆ and SnO₂ in 0.8CSH heterojunction.

As is well-known, under the existence of metal hydroxystannate, the yield of •OH radicals is considered responsible for the photodegradation of organic pollutants [9,37,38]. Fig. 4c exhibits the photoluminescence spectra of the TA solution containing different CSH samples. As expected, for all different CSH samples, a gradual increase in PL intensity at about 425 nm is observed with increase of irradiation time, which confirms the generation of •OH radicals during the photocatalytic reaction. Notably, the

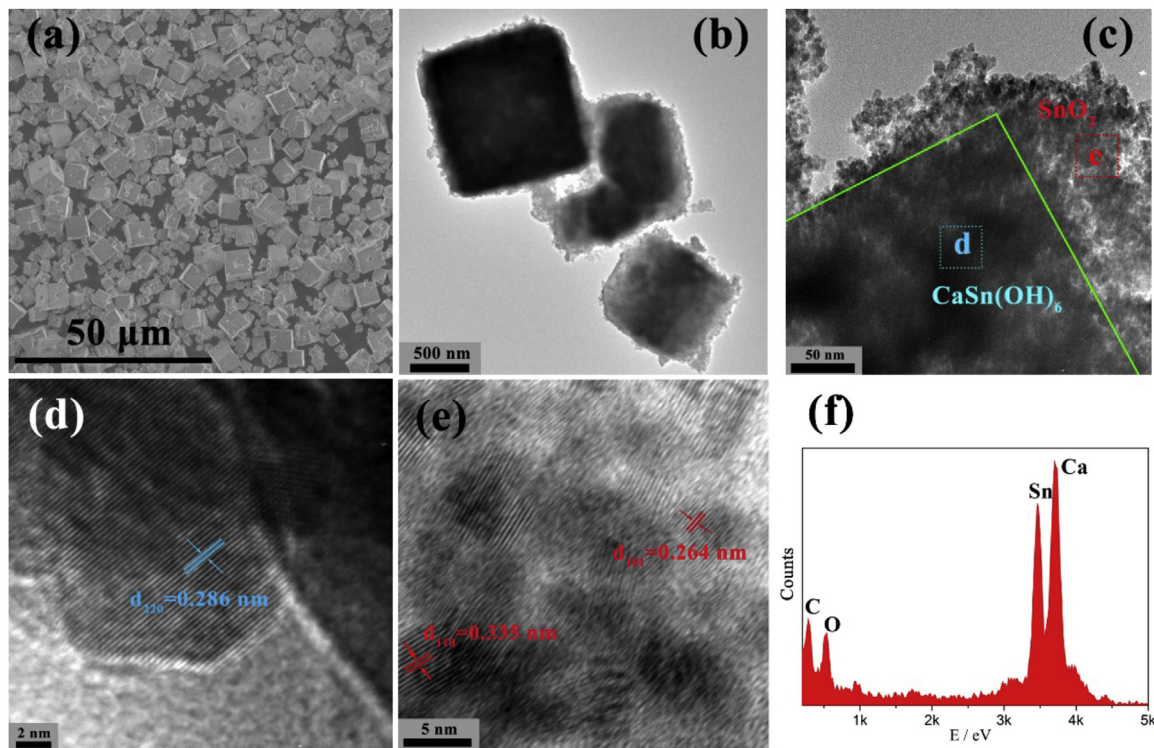


Fig. 3. (a) SEM, (b) Low- and (c) High-magnification TEM images of 0.8CSH cubes. HRTEM images of (d) $\text{CaSn}(\text{OH})_6$ area and (e) SnO_2 area labelled in (c). (f) EDX spectrum of 0.8CSH samples.

increment speed of TAOH produced by 0.8CSH is much higher than that produced by other CSH samples upon excitation at 315 nm. This result indicates that the most $\cdot\text{OH}$ radicals are generated by 0.8CSH sample, which confirms the 0.8CSH has the highest capacity to absorb the converted light for photocatalysis. Furthermore, in order to value the efficiency of charge generation and separation, photocurrents are measured for different CSH samples under UV light irradiation [39]. As shown in Fig. 4d, it is clear that the 0.8CSH electrode exhibits the highest photocurrent value of $10 \mu\text{A}/\text{cm}^2$, which further proves the highest separation ability of photogenerated electrons-holes in 0.8CSH heterojunction, and confirms its great application potential in photocatalytic degradation of pollutant.

Based on the above discussions, the doping of Fe^{3+} ions into CSH has been proceeded with 0.8CSH heterojunction as the target substrate. Fig. 5a shows the XRD patterns of the synthesized FCSH samples at various concentrations of Fe^{3+} ions. As can be seen, all samples are in great agreement with cubic $\text{CaSn}(\text{OH})_6$ (JCPDS 09-0030) and no peaks of impurity phase but SnO_2 presented, which is indicative of the entire dissolution of Fe^{3+} ions into the host lattice. Notably, with the increase of Fe^{3+} ions concentration, the diffraction peaks of FCSH are shifted to higher angles compared with that of standard 0.8CSH, which indicates that Fe^{3+} ions have been effectively incorporated into the 0.8CSH host lattice [40]. This shift of the diffraction position ascribes the changes in the lattice parameters as a result of the different ionic radii between Fe^{3+} (0.064 nm) and Sn^{4+} (0.069 nm). Meanwhile, EDX analysis (Fig. 5b) and full range XPS spectrum (Fig. 5c) collectively confirm the co-existence of Ca, Sn, O and Fe elements in 1.0FCSH samples (as typical samples), which also demonstrate the incorporation of Fe^{3+} into the $\text{CaSn}(\text{OH})_6$. Furthermore, the experimental values of Fe/Ca in the as-synthesized 0.5FCSH, 0.8FCSH, 1.0FCSH and 1.5FCSH samples are determined by ICP-OES (Table 1) to be about 0.37 mol%, 0.82 mol%, 1.03 mol% and 1.44 mol%, respectively, which are close to the theoretical Fe/Ca values. The high resolution XPS spectrum of the $\text{Fe} 2p$ (exhibited in

Table 1
Content of Fe^{3+} ions in different FCSH samples by ICP-OES.

Sample	0.5FCSH	0.8FCSH	1.0FCSH	1.5FCSH
Theoretical content ($\text{Fe}/\text{Ca}\%$)	0.5	0.8	1.0	1.5
Experimental ($\text{Fe}/\text{Ca}\%$)	0.37	0.82	1.03	1.44

Table 2
Band gap energy of 0.8CSH and FCSH synthesized with different concentration of Fe^{3+} ions.

Samples	0.8CSH	0.5FCSH	0.8FCSH	1.0FCSH	1.5FCSH
E_g/eV	3.44	2.86	2.70	2.57	2.49

Fig. 5d) indicates that the peak at 710.5 eV could be assigned to Fe^{3+} ions. Differing from the Fe^{3+} in Fe_2O_3 (at 710.9 eV), the variation in the $\text{Fe} 2p_{3/2}$ level binding energy may be arisen from the formation of Sn–O–Fe bonds in the 1.0FCSH [24]. In addition, morphologies of the as-prepared FCSH samples are displayed in the insert of Fig. 5b and S2. It is observed that the morphologies of the samples have nearly no change with the increase of Fe^{3+} contents, indicating the addition of slight Fe^{3+} ions will not alter the crystal phase structure.

The light-absorbance properties of 0.8CSH and different FCSH samples have been probed with UV-vis absorption spectra, as shown in Fig. 6. 0.8CSH shows a sharp fundamental absorption edge at about 360 nm and no absorbing ability in the visible light region. After introduction of Fe^{3+} ions into 0.8CSH skeleton, the UV-vis absorption spectra of all FCSH samples exhibits a red shift and increased absorption in the visible light region. The higher Fe^{3+} ions content, the greater of red shift grade, which indicates FCSH samples have great potential in photocatalytic degradation of pollutants under visible light irradiation. The direct E_g of different samples are calculated from their absorption spectra based on the previous reports [13,41], and the results are displayed in the inset and tabulated in Table 2. Clearly, the values of E_g decrease

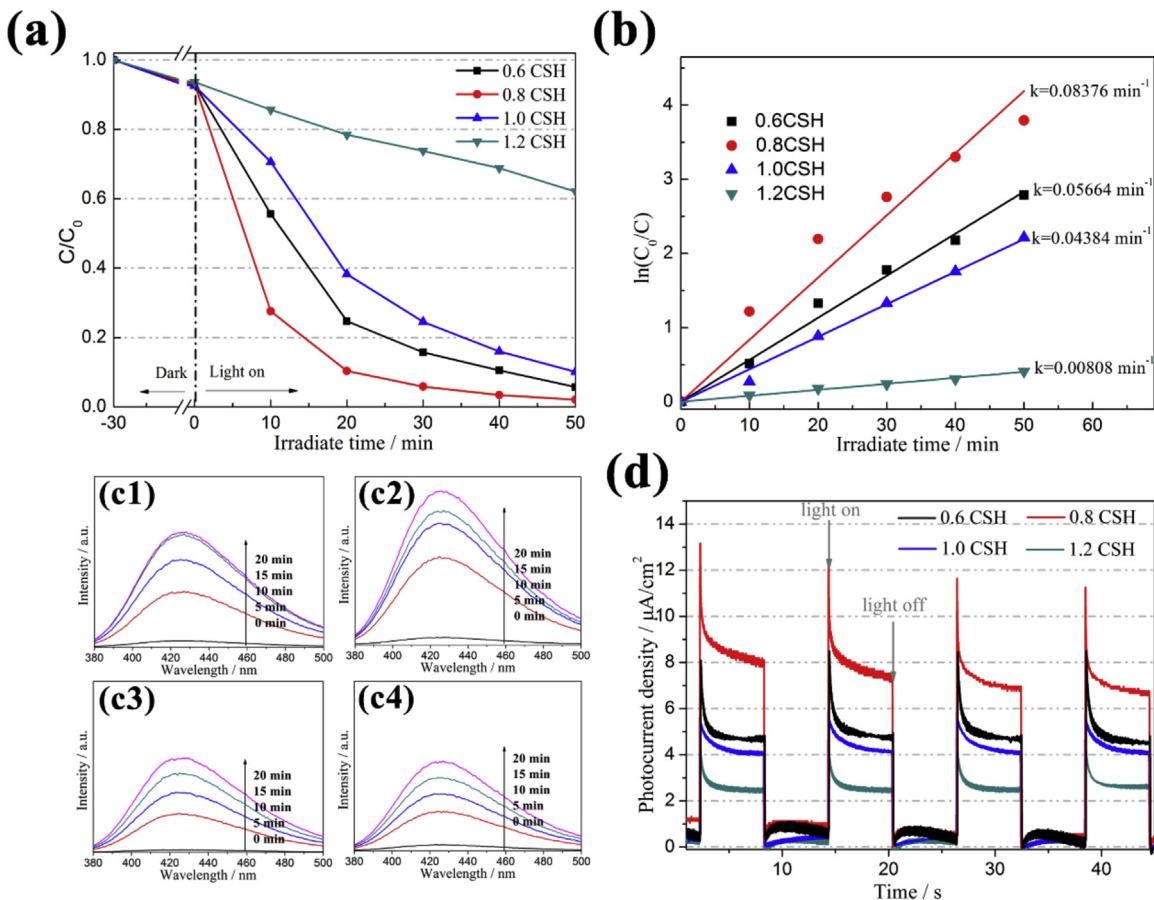


Fig. 4. (a) Variation of MB solution concentration against illumination time in the presence of different CSH samples. (b) Plots of $\ln(C_0/C)$ versus irradiation time for MB solution representing the fit using a pseudo-first-order reaction rate. Fluorescence spectra measured after illumination different time of (c1) 0.6CSH, (c2) 0.8CSH, (c3) 1.0CSH and (c4) 1.2CSH samples in a basic solution of terephthalic acid (TA) (excitation at 315 nm). (d) Photocurrent density vs. time ($I-t$) curves of different CSH samples under UV light illumination conditions.

gradually with the increase of Fe^{3+} contents, which could be attributed to the fact that the doping of Fe^{3+} ions creates dopant levels between the valence band (VB) and conduction band (CB) of CSH. Thus, the photogenerated electrons will transmit from the modified dopant level to the CB more easily, and effectively enhance the photocatalytic activity in visible light region [28,31].

To verify the influence of dopants (Fe^{3+} ions) on the photocatalytic activity, the degradation efficiencies of MB solution under visible light and UV light irradiation are investigated. For comparison, the photocatalytic activity of 0.8CSH has been measured under the same conditions. Before the light irradiation, the suspension will be stirred for 30 min in the dark to reach the adsorption–desorption equilibrium. As shown in Fig. 7a, no photolysis of MB is observed after 5 h visible light irradiation with the absence of photocatalyst, demonstrating the good stability of MB solution under visible light irradiation. The 0.8CSH exhibits nearly no photocatalytic performance under visible light illumination, owing to its large band gap energy of 3.44 eV. By contrast, FCSH samples present much higher photoresponse abilities under irradiation of visible light. Meanwhile, with increasing of Fe^{3+} contents, the photocatalytic efficiency of the FCSH samples increases speedily and reaches a maximum value when Fe^{3+} content is 1.0 mol%. Then, the much higher content of Fe^{3+} in the composite leads to a deterioration of the photocatalytic performance, even though the 1.5FCSH exhibits higher absorption ability in the visible light region. This is due to the fact that the excess Fe^{3+} ions will act as recombination centers through quantum tunneling, and then shorten the lifetime of photogenerated electrons and holes [24]. On the other side, with

regard to UV light induced photodegradation (Fig. 7b), similar phenomena have been observed. For instance, about 92% of the initial MB solution are degraded by 1.0FCSH sample, while only 80% of the initial MB solution are degraded by 0.8CSH within 15 min, i.e., all FCSH samples show higher UV light induced photocatalytic activities than 0.8CSH. These above results effectively prove the doping of Fe^{3+} ions is beneficial to enhance the photocatalytic activities in visible and UV region, and then increase the utilization rate of solar light.

In order to further prove the positive influences of Fe^{3+} ions on the promoted photocatalytic activity, electrical properties of 0.8CSH and different FCSH samples are measured under the selective conditions. The photocurrent responses are carried out under visible light irradiation and shown in Fig. 8a. Clearly, the fast and uniform photocurrent responds are observed within several on-off cycles of intermittent visible light irradiation. As expected, the 0.8CSH sample shows almost no photocurrent response, and the maximal photocurrent values of the FCSH samples increase along with the enhancement in the Fe^{3+} contents from 0 mol% to 1.0 mol%. Nevertheless, the further enhancement of Fe^{3+} content will lead to a decrease in photocurrent value, which is in agreement with the photodegradation quenching under visible light irradiation (Fig. 8a). Furthermore, as for the $I-t$ curves under UV light illumination (Fig. 8b), all of FCSH samples show significant photocurrent intensity enhancements after the modification of Fe^{3+} ions, indicating the higher separation efficiency of the photogenerated electron–hole pairs in FCSH samples.

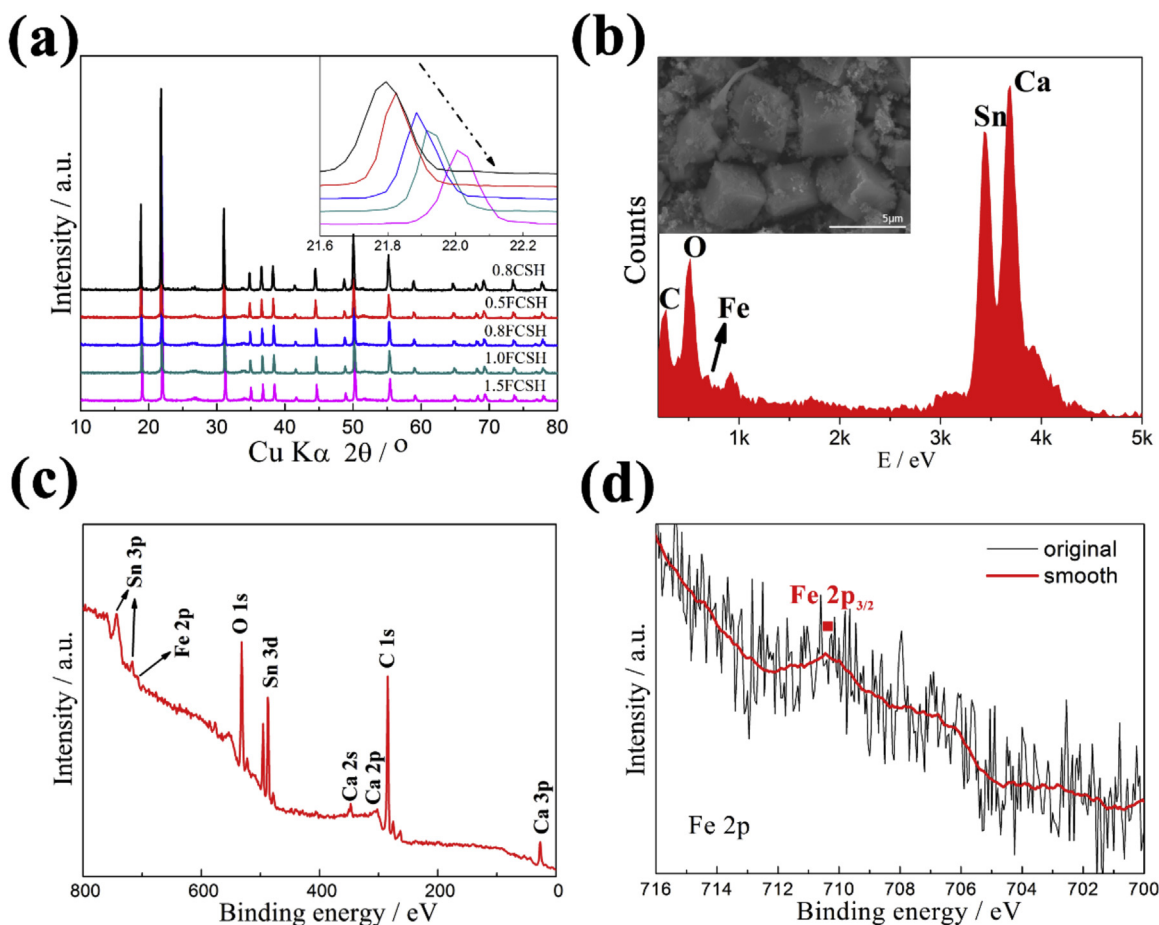


Fig. 5. (a) XRD patterns of FCSH samples synthesized with different concentration of Fe^{3+} ions, and the inset shows XRD patterns from 21.6° to 22.3° . (b) EDX spectrum and SEM image of 1.0FCSH sample. (c) Full range and (d) Fe 2p core-level XPS spectra of the as-prepared 1.0FCSH sample.

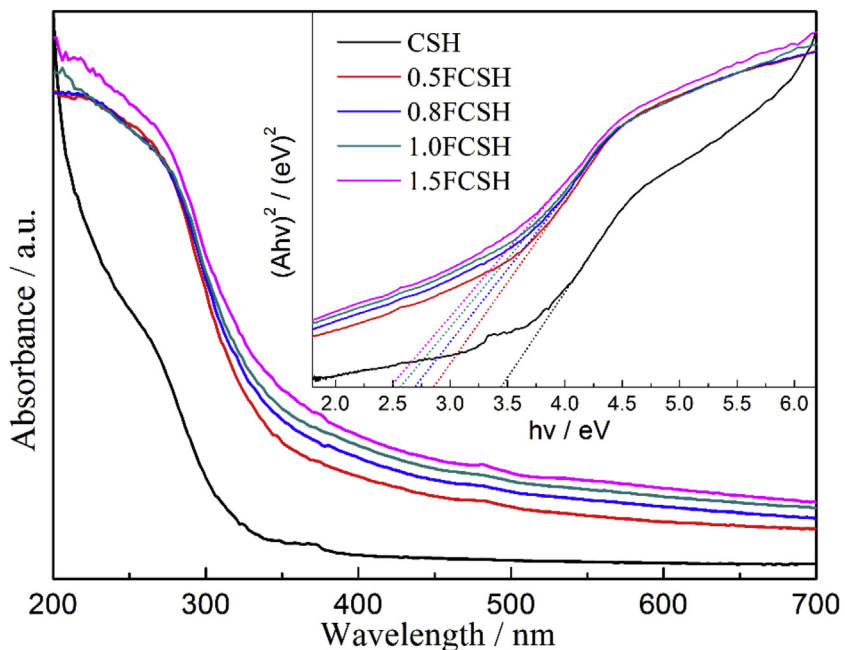


Fig. 6. UV-Vis absorption spectra of FCSH samples synthesized with different concentration of Fe^{3+} ions. The inset shows the plots of $(\text{Ahv})^2$ versus photo energy for band gap energy (E_g).

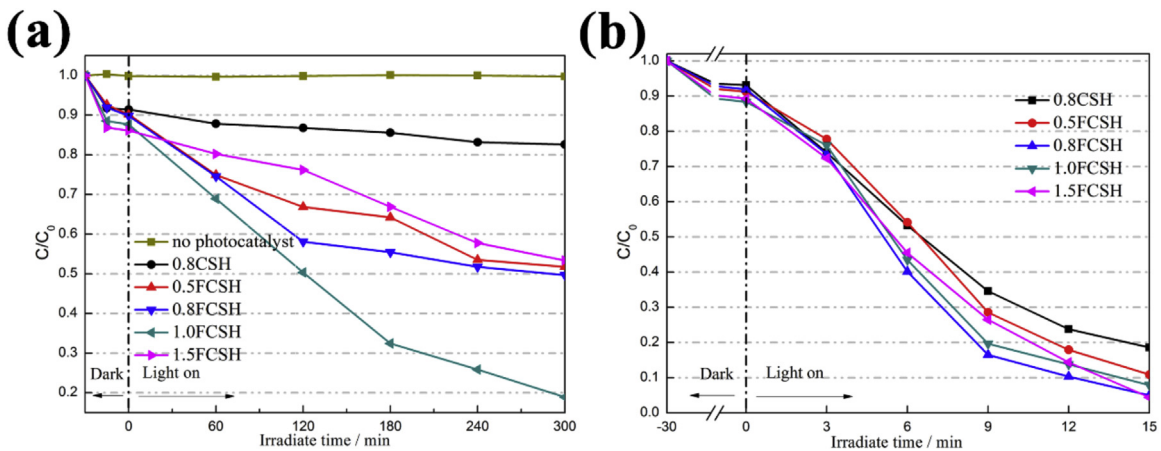


Fig. 7. Variation of MB solution concentration against irradiation time using 0.8CSH and different FCSH samples under (a) visible light and (b) UV light irradiation.

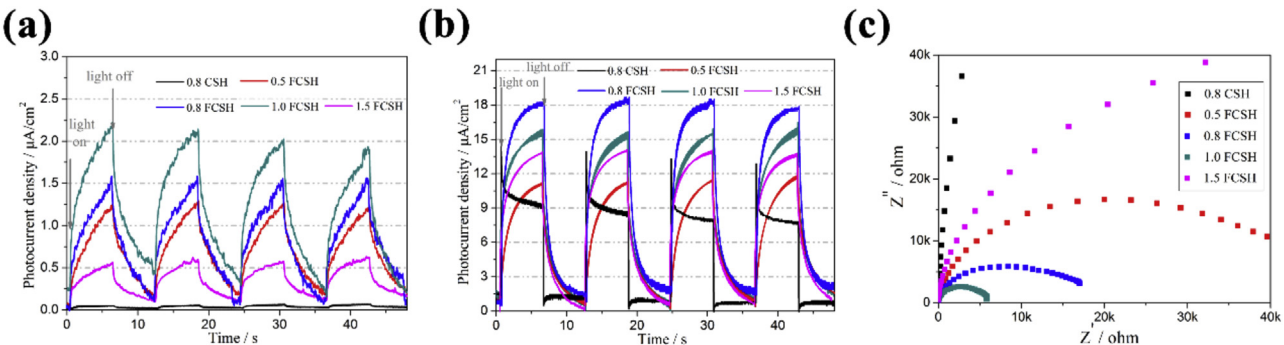


Fig. 8. Photocurrent density vs. time ($I-t$) curves of 0.8CSH and different FCSH samples under (a) visible light and (b) UV light illumination conditions. (c) EIS Nyquist plots of 0.8CSH and different FCSH samples in the dark.

Meanwhile, EIS is employed to investigate the process of electron transfer in different samples, and the reaction rate occurring on the working electrode surface is reflected by the arc radius. As shown in Fig. 8c, all of FCSH samples show smaller radiiuses of the Nyquist circle than 0.8CSH sample, and the 1.0FCSH exhibits the smallest arc radius. These results not only indicate the positive effects of the doping of Fe^{3+} ions, but also confirm the fastest interfacial charge transfer and the most effective separation of electron-hole pairs in the 1.0FCSH sample, which are beneficial for its enhanced photocatalytic activity.

In order to elucidate the photocatalytic mechanism, reactive species trapping experiments are carried out in the presence of 0.8CSH or 1.0FCSH samples under UV or visible light irradiation. As shown in Fig. 9a, the photocatalytic efficiency of 0.8CSH decreases distinctly no matter with the addition of EDTA-2Na (h^+ scavenger), $t\text{-BuOH}$ ($\cdot\text{OH}$ scavenger) or BQ ($\cdot\text{O}_2^-$ scavenger), indicating all three reactive species make contributions to the degradation of MB solution with existence of 0.8CSH. With regard to 1.0FCSH, the degradation efficiency decreases slightly with the addition of EDTA-2Na and $t\text{-BuOH}$ but obviously with the addition of BQ. Furthermore, photoluminescence method is used with TA as a probe (Fig. 9c), and the generated PL intensity indicates the $\cdot\text{OH}$ radicals produced during the photocatalytic reaction. These results indicate the photogenerated $\cdot\text{O}_2^-$ radical is the main active species while h^+ and $\cdot\text{OH}$ radicals play assistant roles on the degradation of MB solution. Therefore, even if the oxidative species contribution may change a little after doping Fe^{3+} ions into 0.8CSH skeleton, all reactive species (h^+ , $\cdot\text{OH}$ and $\cdot\text{O}_2^-$) play important roles in the photocatalytic degradation under UV light irradiation. As for the trapping experiment over 1.0FCSH under visible light irradiation

(Fig. 9b), the photodegradation efficiency has nearly no change when the $t\text{-BuOH}$ is added, while the addition of EDTA-2Na and BQ results in the fast deactivation of 1.0FCSH photocatalyst. These results indicate that the photogenerated h^+ and $\cdot\text{O}_2^-$ are the main oxidative species while $\cdot\text{OH}$ radicals no longer contribute to the photocatalytic process, which differs from that under UV light illumination. Meanwhile, nearly no signal of $\cdot\text{OH}$ radicals is detected for 1.0FCSH upon visible light irradiation (Fig. 9d), further indicating that no $\cdot\text{OH}$ radicals is produced in the visible light induced photocatalytic process.

On the basis of the above experimental results and the theory analysis, schematic diagrams of the $\text{CaSn}(\text{OH})_6\text{-SnO}_2$ heterojunction and FCSH samples are illustrated in Fig. 10. To clarify the position of CB of $\text{CaSn}(\text{OH})_6$, the flat-band potential (V_{fb}) has been carried out and the result is displayed in Fig. S3. Clearly, the V_{fb} of pure $\text{CaSn}(\text{OH})_6$, as calculated from the x intercepts of the linear region, is estimated to be -0.18 V vs. NHE [42], thus the CB of $\text{CaSn}(\text{OH})_6$ is -0.38 V vs. NHE [43]. Furthermore, combining with the band gap energy of $\text{CaSn}(\text{OH})_6$ as shown in Fig. 6 (3.44 eV) and the reported band potentials of SnO_2 ($E_{\text{VB}} = -3.6$ V vs. NHE, $E_{\text{CB}} = 0$ V vs. NHE) [21], the energy level diagrams and charge-transfer processes of $\text{CaSn}(\text{OH})_6\text{-SnO}_2$ heterojunction are displayed in Case I (Fig. 10). Because of the wide band gap energy of $\text{CaSn}(\text{OH})_6$ and SnO_2 , both of them only could be excited by UV light to generate electrons and holes. Meanwhile, the electron transfer occurs from the CB of $\text{CaSn}(\text{OH})_6$ to that of SnO_2 while the photogenerated holes transfer from the VB of SnO_2 to that of $\text{CaSn}(\text{OH})_6$. Under this circumstance, the efficient separation of photogenerated electrons and holes leads to the increased lifetime of charge carriers, thus enhances the UV light induced photocatalytic activity. As dis-

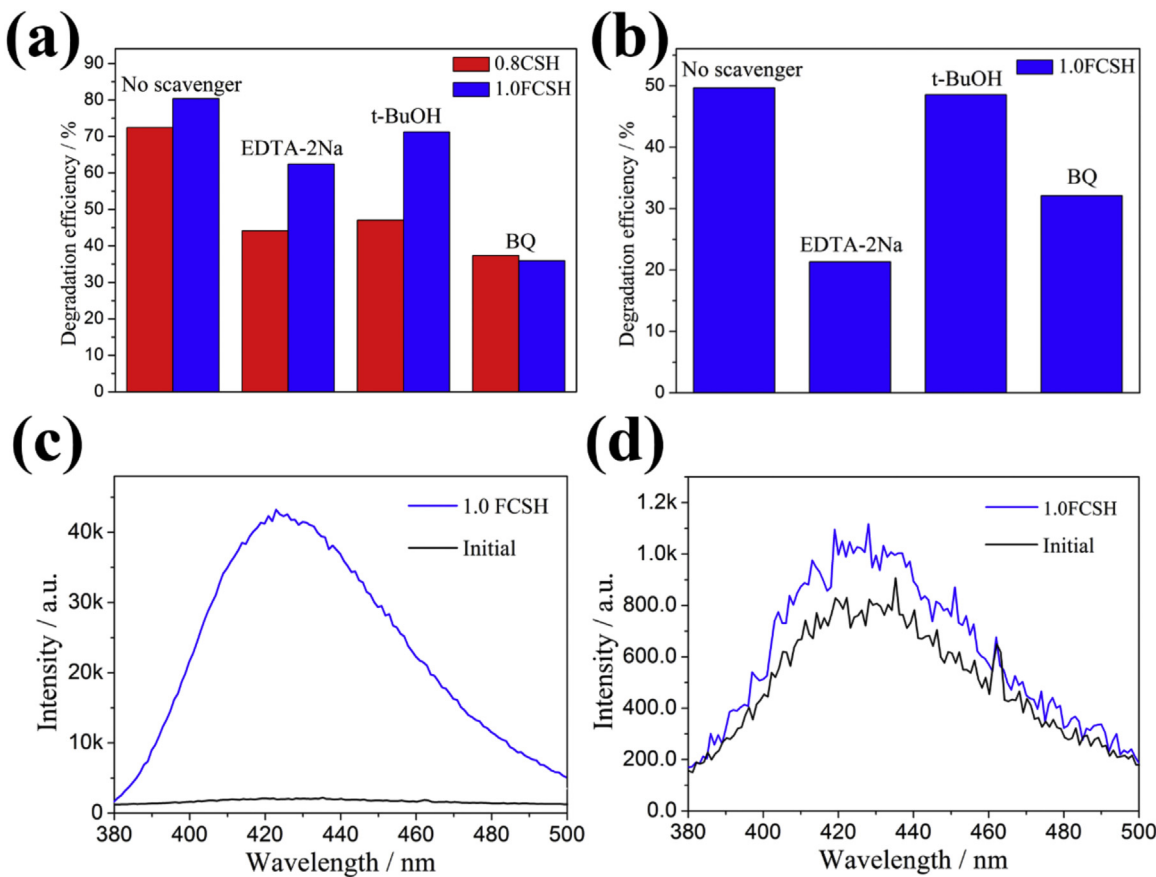


Fig. 9. Degradation efficiency of MB solution by using different radical scavengers for (a) 0.8CSH and 1.0FCSH under UV light irradiation and (b) 1.0FCSH under visible light irradiation. Fluorescence spectra of 1.0FCSH measured after (c) UV light illumination 20 min and (d) visible light illumination 30 min in a basic solution of TA (excitation at 315 nm).

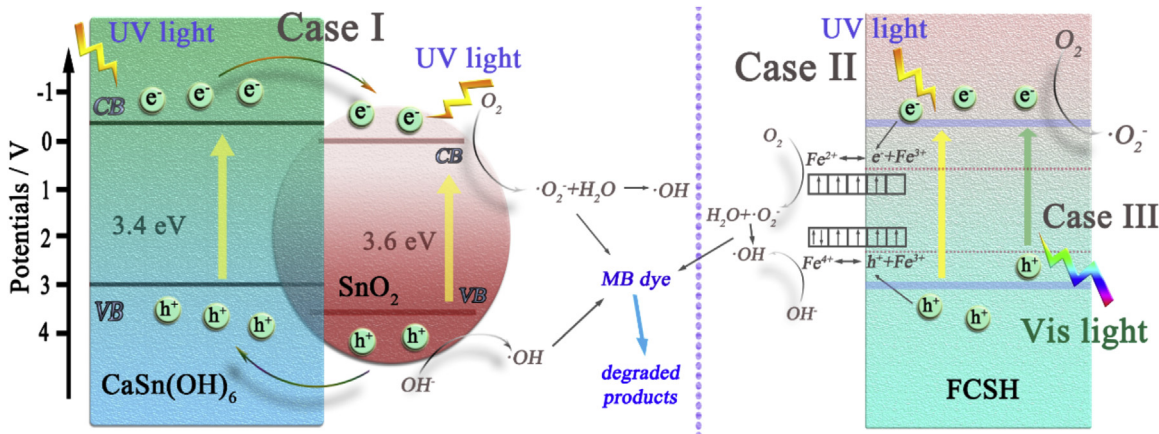
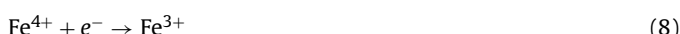


Fig. 10. Proposed mechanism for the photogenerated electron–hole separation and transport processes in CaSn(OH)₆–SnO₂ heterojunction and FCSH samples under UV light or visible light irradiation.

played in Case II (Fig. 10), after the doping of Fe³⁺ ions into the 0.8CSH substrate, dopant levels will be created between the CB and VB of the substrate, and then increase the absorption intensity of UV light and visible light (Eq. (2)). Due to the fact that the energy level of Fe³⁺/Fe²⁺ (0.77 V vs. NHE) is below the CB of CaSn(OH)₆ and the energy level of Fe⁴⁺/Fe³⁺ (2.20 V vs. NHE) is above the VB of CaSn(OH)₆ [40], Fe³⁺ ions can act as both electrons acceptor (from Fe³⁺ to Fe²⁺, Eq. (3)) and holes donor (from Fe³⁺ to Fe⁴⁺, Eq. (4)). In addition, the half-filled 3d⁵ orbit of Fe³⁺ implies its higher stability than Fe²⁺ and Fe⁴⁺. Hence, the trapped electrons trend to escape

from Fe²⁺ (Eq. (5)) while Fe⁴⁺ adsorbs surface hydroxyl (OH⁻, Eq. (6)). In this situation, some active species like •O₂⁻ and •OH will be generated plenty under the irradiation of UV light, which can further degrade MB dye to non-toxic substance. Under the circumstances, the doping of Fe³⁺ ions inhibits the recombination of photo-generated charge carriers and further promotes the photocatalytic activity under UV light irradiation [44,45]. On the other side, under the illumination of visible light (Case III in Fig. 10), the electrons can be excited from the dopant level (Fe⁴⁺/Fe³⁺) to the CB of FCSH photocatalysts. As we know, the energy level of Fe⁴⁺/Fe³⁺

(2.20 V vs. NHE) is more negative than that of $\cdot\text{OH}/\text{H}_2\text{O}$ (2.32 V vs. NHE) [17], which suggests that the photogenerated holes on the surface of FCSH will accelerate the decomposition of organic pollutants into degraded products, rather than generate the stronger oxidative species ($\cdot\text{OH}$). Moreover, with the excess increasement of Fe^{3+} ions contents (more than 1.0 mol%), more and more Fe^{3+} ions will be mainly doped at the major depth below the surface, and serve as a recombination center (Eqs. (7) and (8)), resulting in the decrease of photocatalytic activity [41,45]. The detailed reaction steps are as follows:



From the viewpoint of practical application, the recycling of the 1.0FCSH photocatalyst is generally required. As shown in Fig. S4a, after four runs for the photocatalytic degradation of MB solution, no apparent deactivation of the 1.0FCSH photocatalyst is observed, indicating the high stability and long-term use of FCSH photocatalysts in the photocatalytic reaction process. Since the FCSH is a metastable phase (hydroxystannate), the thermostability study for photocatalyst is needed and it has been carried out by TGA experiment (Fig. S4b) [46]. It is found that 1.0FCSH starts to decompose (accompanied with obvious weight loss) at about 254 °C, which is much higher than operating temperature of photocatalysts. This result further indicates the widespread applicability of FCSH samples in photocatalysis.

4. Conclusion

In summary, the novel CSH heterostructure photocatalysts have been realized successfully via a one-pot hydrothermal method first. Owing to the fact that the formation of appropriate $\text{CaSn}(\text{OH})_6\text{-SnO}_2$ heterojunction can accelerate the separation of photogenerated electron-hole pairs, the optimal samples (0.8CSH) show much higher photocatalytic activity under UV light irradiation compared with $\text{CaSn}(\text{OH})_6$. Furthermore, highly efficient FCSH samples are designed and synthesized via doping Fe^{3+} ions into 0.8CSH substrate. The formation of dopant level in CSH lattice resulting in the decreased recombination rate of photogenerated carriers and the pronounced photoresponse in the visible light region, which are beneficial to the photocatalytic reaction. By optimizing the Fe^{3+} ions content, the as-prepared FCSH samples display greatly enhancement in the decomposition of MB solution under the irradiation of visible light and UV light. In addition to higher photocatalytic activities, this work also provides a promising strategy in the preparation and modification of metal hydroxystannate materials, which may have potential applications in energy conversion and environmental protection.

Acknowledgements

This research is supported by the Fundamental Research Funds for the Central Universities (Izujbky-2016-129), the International Sci. & Tech. Cooperation Foundation of Gansu Provincial, China (Grant Nos 1504WKCA088), and the Gansu Province Development and Reform Commission (NDRC, No. 2013-1336).

Appendix A. Supplementary data

Supplementary data associated with this article can be found, in the online version, at <http://dx.doi.org/10.1016/j.apcatb.2017.05.080>.

References

- [1] A. Iwase, S. Yoshino, T. Takayama, Y.H. Ng, R. Amal, A. Kudo, *J. Am. Chem. Soc.* 138 (2016) 10260–10264.
- [2] S. Sun, W. Wang, D. Jiang, L. Zhang, X. Li, Y. Zheng, Q. An, *Nano Res.* 7 (2014) 1497–1506.
- [3] X. Ma, H. Li, T. Liu, S. Du, Q. Qiang, Y. Wang, S. Yin, T. Sato, *Appl. Catal. B: Environ.* 201 (2017) 348–358.
- [4] S. Ouyang, H. Tong, N. Umezawa, J. Cao, P. Li, Y. Bi, Y. Zhang, J. Ye, *J. Am. Chem. Soc.* 134 (2012) 1974–1977.
- [5] A. Iwase, H. Kato, A. Kudo, *Appl. Catal. B: Environ.* 136–137 (2013) 89–93.
- [6] W. Ji, K. Yao, Y.-F. Lim, Y.C. Liang, A. Suwardi, *Appl. Phys. Lett.* 103 (2013) 062901.
- [7] G. Zhang, G. Liu, L. Wang, J.T. Irvine, *Chem. Soc. Rev.* 45 (5951) (2016) 21.
- [8] H. Li, S. Yin, Y. Wang, T. Sato, G. Rohrer, *J. Am. Ceram. Soc.* 96 (2013) 1258–1262.
- [9] T. Yan, X. Wang, J. Long, P. Liu, X. Fu, G. Zhang, X. Fu, *J. Colloid Interface Sci.* 325 (2008) 425–431.
- [10] E.M. Seftel, E. Popovici, M. Mertens, K.D. Witte, G.V. Tendeloo, P. Cool, E.F. Vansant, *Microporous Mesoporous Mater.* 113 (2008) 296–304.
- [11] C.G. Silva, Y. Bouizi, V. Fornés, H. García, *J. Am. Chem. Soc.* 131 (2009) 13833–13839.
- [12] X. Fu, X. Wang, Z. Ding, D.Y.C. Leung, Z. Zhang, J. Long, W. Zhang, Z. Li, X. Fu, *Appl. Catal. B: Environ.* 91 (2009) 67–72.
- [13] E.S. Baeissa, *J. Alloys Compd.* 590 (2014) 303–308.
- [14] S. Moshtaghi, M. Salavati-Niasari, D. Ghanbari, *J. Nanostruct.* 5 (2015) 169–174.
- [15] S. Meng, D. Li, M. Sun, W. Li, J. Wang, J. Chen, X. Fu, G. Xiao, *Catal. Commun.* 12 (2011) 972–975.
- [16] Z. Zhang, C. Shao, X. Li, L. Zhang, H. Xue, C. Wang, Y. Liu, *J. Phys. Chem. C* 114 (2010) 7920–7925.
- [17] T. Liu, B. Liu, L. Yang, X. Ma, H. Li, S. Yin, T. Sato, T. Sekino, Y. Wang, *Appl. Catal. B: Environ.* 204 (2017) 593–601.
- [18] H. Li, Y. Zhou, W. Tu, J. Ye, Z. Zou, *Adv. Funct. Mater.* 25 (2015) 998–1013.
- [19] L. Zhang, H. Zhang, H. Huang, Y. Liu, Z. Kang, *New J. Chem.* 36 (2012) 1541.
- [20] Y.C. Zhang, Z.N. Du, K.W. Li, M. Zhang, D.D. Dionysiou, *ACS Appl. Mater. Interfaces* 3 (2011) 1528–1537.
- [21] L. Xu, E.M.P. Steinmiller, S.E. Skrabalak, *J. Phys. Chem. C* 116 (2012) 871–877.
- [22] J. Tian, Y. Leng, Z. Zhao, Y. Xia, Y. Sang, P. Hao, J. Zhan, M. Li, H. Liu, *Nano Energy* 11 (2015) 419–427.
- [23] M.T. Uddin, Y. Nicolas, C. Olivier, T. Toupance, L. Servant, M.M. Muller, H.J. Klebe, J. Ziegler, W. Jaegermann, *Inorg. Chem.* 51 (2012) 7764–7773.
- [24] J. Yu, Q. Xiang, M. Zhou, *Appl. Catal. B: Environ.* 90 (2009) 595–602.
- [25] R. Ullah, J. Dutta, J. Hazard. Mater. 156 (2008) 194–200.
- [26] S.-m. Chang, W.-s. Liu, *Appl. Catal. B: Environ.* 101 (2011) 333–342.
- [27] M. Zhou, J. Yu, B. Cheng, J. Hazard. Mater. 137 (2006) 1838–1847.
- [28] H. Song, Y. Li, Z. Lou, M. Xiao, L. Hu, Z. Ye, L. Zhu, *Appl. Catal. B: Environ.* 166–167 (2015) 112–120.
- [29] J.-H. Lee, B.-O. Park, *Thin Solid Films* 426 (2003) 94–99.
- [30] A.R. Bally, E.N. Korobeinikova, P.E. Schmid, F. Lévy, F. Bussy, *J. Phys. D: Appl. Phys.* 31 (1998) 1149.
- [31] X. Yang, C. Cao, L. Erickson, K. Hohn, R. Maghirang, K. Klabunde, *Appl. Catal. B: Environ.* 91 (2009) 657–662.
- [32] W. Wang, J. Bi, L. Wu, Z. Li, X. Fu, *Scr. Mater.* 60 (2009) 186–189.
- [33] M.-C. Daniel, D. Astruc, *Chem. Rev.* 104 (2004) 293–346.
- [34] S. Kumar, T. Surendar, A. Baruah, V. Shanker, *J. Mater. Chem. A* 1 (2013) 5333.
- [35] J.X. Sun, Y.P. Yuan, L.G. Qiu, X. Jiang, A.J. Xie, Y.H. Shen, J.F. Zhu, *Dalton Trans.* 41 (2012) 6756–6763.
- [36] T. Liu, B. Liu, J. Wang, L. Yang, X. Ma, H. Li, Y. Zhang, S. Yin, T. Sato, T. Sekino, Y. Wang, *Sci. Rep.* 6 (2016) 27373.
- [37] Z. Li, Z. Xie, Y. Zhang, L. Wu, X. Wang, X. Fu, *J. Phys. Chem. C* 111 (2007) 18348–18352.
- [38] D. Huang, X. Fu, J. Long, X. Jiang, L. Chang, S. Meng, S. Chen, *Chem. Eng. J.* 269 (2015) 168–179.
- [39] S.G. Babu, V. Ramalingam, B. Neppolian, D.D. Dionysiou, M. Ashokkumar, *J. Hazard. Mater.* 291 (2015) 83–92.
- [40] D. Channei, B. Inceesungvorn, N. Wetchakun, S. Ukrinunkun, A. Nattestad, J. Chen, S. Phanichphant, *Sci. Rep.* 4 (2014) 5757.
- [41] L. Sun, J. Li, C.L. Wang, S.F. Li, H.B. Chen, C.J. Lin, *Sol. Energy Mater. Sol. Cells* 93 (2009) 1875–1880.
- [42] S.J. Hong, S. Lee, J.S. Jang, J.S. Lee, *Energy Environ. Sci.* 4 (2011) 1781.
- [43] H. Yang, J. Tian, T. Li, H. Cui, *Catal. Commun.* 87 (2016) 82–85.
- [44] S. Tonda, S. Kumar, S. Kandula, V. Shanker, *J. Mater. Chem. A* 2 (2014) 6772.
- [45] T. Tong, J. Zhang, B. Tian, F. Chen, D. He, *J. Hazard. Mater.* 155 (2008) 572–579.
- [46] X. Fu, D. Huang, Y. Qin, L. Li, X. Jiang, S. Chen, *Appl. Catal. B: Environ.* 148–149 (2014) 532–542.